Biogas upgrading for on-board hydrogen production: Reforming process CFD modelling International Journal of Hydrogen Energy

Hamedi, Mohammadreza; Tsolakis, Athanasios; Lau, Chia-Sheng

DOI:
10.1016/j.ijhydene.2014.06.017

Biogas upgrading for on-board hydrogen production: Reforming process CFD modelling

M.R. Hamedi, A. Tsolakis[1], C.S. Lau

School of Mechanical Engineering, University of Birmingham, Birmingham B15 2TT, UK

Abstract

Hydrogen production through fuel reforming can be used to improve IC (internal combustion) engines combustion characteristics and to lower vehicle emissions. In this study, a computational fluid dynamics (CFD) model based on a detailed kinetic mechanism was developed for exhaust gas reforming of biogas to synthetic gas (H_2 and CO). In agreement with experimental data, the reactor's physical and chemical performance was investigated at various O_2/CH_4 ratios and gas hourly space velocities (GHSV). The numerical results imply that methane reforming reactions are strongly sensitive to O_2/CH_4 ratio and engine exhaust gas temperature. It was also found that increasing GHSV results in lower hydrogen yield; since dry and steam reforming reactions are relatively slow and are both dependent on the flow residence time. Furthermore, the hot spot effect, which is associated to oxidation reforming reactions, was investigated for catalyst activity and durability.

Keywords: Biogas upgrade; Fuel reforming; Hydrogen; CFD; Reaction kinetics.

[1] Corresponding author. Tel.: +44 121 414 4170; fax: +44 121 414 7484.
E-mail address: a.tsolakis@bham.ac.uk (A. Tsolakis).

1. Introduction

Biogas, which is produced through the anaerobic degradation of organic materials, can be used to reduce energy related pollution. Biogas typically contains 55-65% methane and 35-45% carbon dioxide (CO_2) and can be produced from different biomass waste and landfill materials [1]. Thus biogas has the advantage of being both clean and renewable along with an ease of implementation in existing power generating systems and to a less extent in transportation [2, 3].

For automotive applications, biogas fuelled internal combustion (IC) engines can be used; however, in addition to challenges associated with on-board storage, they also suffer from combustion instability and high unburned methane emissions [4]. Moreover, the CO_2 content of the biogas, which dilutes the intake charge, limits the engine peak power due to the decrease in fuel calorific value. Several studies have reported that the addition of hydrogen to the intake mixture is beneficial for IC engines, since it can break the NO_x-particulate trade-off, promote auto-ignition, improve combustion stability and enhance after-treatment systems activity [5]. Since storing hydrogen is as yet impractical, attention has been recently given to on-board generation of hydrogen using reforming processes such as the exhaust gas reforming process proposed here (Fig. 1).

In this process, also known as REGR, exhaust gas heat is utilised to reform a mixture of fuel and exhaust gas into synthetic gas (H_2 and CO) over a precious metal catalyst. The hydrogen enriched gas is then injected into the engine manifold to be mixed with intake air. Several studies have proven that REGR improves combustion characteristics and decreases particulate and NO_x emissions, as well [5, 6]. The inherent complexity of REGR requires

appropriate modelling in order to optimise its implementation; this in turn requires a deep insight into the chemical and physical behaviour of its processes.

Fuel reforming reactions are complicated and still a matter of debate in the literature. Four main global reactions contribute to the catalytic reformation of methane; namely dry reforming (DRR, Eq. 1); partial oxidation (POX, Eq. 2); steam reforming (SRR, Eq. 3) and water gas shift reaction (WGSR, Eq. 4). Although methane SRR is the most versatile method for H_2 production, POX offers a promising alternative for automotive applications since its exothermic nature provides heat for accelerating other endothermic reactions. Furthermore, partial oxidation is a suitable process for small scale applications and allows a compact reactor design. On the other hand, in POX reactors, the presence of hot spots near the catalyst entrance can considerably affect the catalyst durability [7].

While the number of global reactions in methane reforming is limited, there are several elementary reactions that have to be taken into account for its accurate kinetic modelling. According to Dalle Nogare, “Since both exothermic and endothermic reactions are involved, a temperature variation does not translate directly to a reactant conversion, and energy and mass balance are deeply coupled” [8]. This indicates that computational fluid dynamics (CFD) is a valuable tool for reforming process modelling in comparison to plug flow reactor (PFR) models, where heat and mass transport is simplified excessively.

Dry reforming reaction

$$\mathrm{CH_4 + CO_2 \rightarrow 2CO + 2H_2} \quad (\Delta \mathrm{H_r} = +260.6\ \mathrm{kJ/mol}) \tag{1}$$

Partial oxidation reforming

$$\mathrm{CH_4 + 0.5O_2 \rightarrow CO + 2H_2} \quad (\Delta \mathrm{H_r} = -22.63\ \mathrm{kJ/mol}) \tag{2}$$

Steam reforming reaction

$$CH_4 + H_2O \rightarrow CO + 3H_2 \quad (\Delta H_r = +226.8\ \mathrm{kJ/mol}) \tag{3}$$

Water gas shift reaction

$$CO + H_2O \rightarrow CO_2 + H_2 \quad (\Delta H_r = -33.86\ \mathrm{kJ/mol}) \tag{4}$$

To date, most research on methane reforming has been focused on applications related to fuel cell and fuel processing for instance Fischer-Tropsch and GTL (gas to liquid). Therefore hydrogen purity and optimizing H_2/CO ratio were the major parameters to consider [9]. However, in REGR there is a major difference which requires further investigation. The transient nature of the exhaust gas conditions requires a responsive design for an REGR reactor to obtain a satisfactory hydrogen yield. This can be achieved by understanding the effect of different key parameters such as O_2/CH_4 ratio, inlet temperature, etc.

In this study, a three dimensional CFD model for a heterogeneous POX reactor with a rhodium catalyst was developed. A detailed kinetic model, proposed by Deutschmann et al. was adapted for simulating the reforming surface reactions [10]. The model was validated with the experimental results published in our earlier work [11]. The validated model was used to investigate the overall performance of biogas reforming at various operating conditions. The effect of different O_2/CH_4 ratios was examined to optimize the exhaust gas (as the source of oxygen) contribution in the reactor feed gas. Moreover, the influence of gas hourly space velocity (GHSV, Eq. 5) was also investigated in order to study the influence of various flow rates on the R-EGR system. Simulated operating conditions are detailed in Table 1.

$$\mathrm{GHSV}(h^{-1}) = \frac{1}{\text{Residence time}} = \frac{\text{Feed flow rate}(m^3 h^{-1})}{\text{Catalyst bed volume}(m^3)} \tag{5}$$

2. Methodology

2.1. Reactor geometry and CFD grid

The geometry of the model, which is illustrated schematically in Fig. 2, was created based on the monolith reactor used by Lau et al. [11]. The biogas reforming reactor was modelled as an isothermal heterogeneous reactor. It consists of two zones which are connected at an interface, namely a heat up zone and a monolith zone. The reactant temperature increases while passing through the non-reactive heat up zone. Inside the monolith zone reforming surface reactions occur with the presence of the rhodium catalyst.

For simulation purposes, only a single quarter of the geometry was modelled assuming horizontal and vertical symmetry planes at x=0 and y=0, respectively. The reactor wall is considered to be at a constant temperature (isothermal) since it was held within a large tube furnace in the experimental study [11]. It should be noted that in the REGR application, the reactor would be integrated in a heat exchanger to gain thermal energy from the main stream of the engine exhaust gas to accelerate the reforming reactions. The geometry was discretized into 25,680 structured hexagonal cells using the sweep method in ANSYS ICEM CFD software (ANSYS Inc.). Grid density was increased near the catalyst entrance where higher temperature and species gradients exist. To ensure that the results are grid-independent, the number of elements was increased to 39,462 and a maximum difference of 0.3% in hydrogen molar concentration was observed.

2.2. Governing equations

According to the experiment by Lau et al. [12] the GHSV values were set at 16,500 h^{-1} and 25,500 h^{-1}, which corresponds to Reynolds number of approximately Re=72 and Re=111, respectively. Therefore the flow was assumed to be laminar and inertial forces were neglected. The gas mixture is also assumed to be Newtonian, incompressible and ideal. The conservation equations for continuity (Eq. 6), momentum (Eq. 7), energy (Eq. 8) and species (Eq. 9) are considered as:

$$\nabla.(\rho\vec{v}) = 0 \tag{6}$$

$$\nabla.(\rho\vec{v}\vec{v}) = -\nabla p + F \tag{7}$$

$$\nabla.\left(\vec{v}\,(\rho E + p)\right) = -\nabla.\left(\sum_{i=1}^{N} h_i J_i\right) + S_h \tag{8}$$

$$\nabla.(\rho\vec{v}\,X_i) = -\nabla.\,\vec{J_i} + R_i + S_i \tag{9}$$

Radiation heat transfer was neglected because its effect is insignificant at low temperatures (below 1000 ºC). The dependence of mixture specific heat capacity on temperature was taken into account by polynomial curve fitting from an available thermodynamic database. Mixture mass diffusivity was computed based on the kinetic theory, while its viscosity was calculated by using mixing law.

2.3. Catalyst

Several researchers have previously carried out one-dimensional simulations of the monolith; however, in this approach the effect of radial heat transfer was neglected [7, 8]. In

the current study, the monolith zone was considered as a porous media consisting of both gaseous and solid phases. Therefore axial and radial heat transfer in both phases was taken into account to achieve higher accuracy. The ratio of gas phase volume to total volume was defined as porosity and it was calculated to be 0.78.

Heat conduction in the solid structure of the monolith redirects the heat to the upstream regions and contributes to further pre-heating of the reacting mixture. Based on the catalyst used by Lau et al. [12] a thermal conductivity of 2.25 W m^{-1} K^{-1} was estimated for the solid phase, which is a typical value for a ceramic monolith (e.g. cordierite and zirconium oxide). The catalyst active sites were made of rhodium and the site density (Γ) was assumed to be 2.7×10^{-5} mol m^{-2}.

2.4. Reactants composition

In the exhaust gas fuel reforming process the reactor inlet feed is a mixture of fuel and engine exhaust gas. This mixture is also used to utilise part of the exhaust gas energy and provide oxygen for the catalytic oxidation reactions. The exhaust gas composition used in this study is presented in Table 2. The biogas composition in this case consisted of 60% CH_4 and 40% CO_2. The reactor inlet composition at different O_2/CH_4 ratios is also presented in Table 2. The inlet mixture temperature was set at 300 $^{\circ}$C for the entire test conditions, which is a typical diesel engine exhaust gas temperature. The reactor inlet velocity was also calculated at different gas hourly space velocities based on Eq. 5.

2.5. Reaction mechanism

Methane reforming kinetics is complex, even though the methane molecular configuration is the simplest of the hydrocarbons. As pointed out previously, four main global reactions contribute to the catalytic reformation of methane; however, for accurate kinetic modelling these reactions should be adapted into several elementary steps. In the case of heterogeneous reactions, the gas phase species are first adsorbed onto the catalyst surface and then the main reactions occur followed by desorption [13].

In this study, a detailed kinetic model was used to simulate the reactions inside the monolith zone. The model, which includes a 38-step mechanism to describe the surface reactions, is presented in Table 3 [10]. This mechanism involves 6 gas phase species and 12 surface adsorbed species.

On considering a reaction mechanism that includes N_g gas species, N_s surface species and k_s elementary reactions, the rate of depletion or creation of species i is calculated as:

$$R_i = \sum_{k=1}^{k_s} \upsilon_{i,k} k_{f,k} \prod_{j=1}^{N_g+N_s} [X_j]^{\upsilon_{j,k}} \quad (i = 1, \dots, N_g + N_s) \tag{10}$$

Where υ is the stoichiometric coefficient and X_j, which is the molar concentration of species j, is defined as:

$$[X_j] = \Gamma \Theta_j \tag{11}$$

Where Θ_j is the surface coverage of species j. $k_{f,k}$ (the forward reaction rate) is calculated by the modified Arrhenius equation based on the reactor's local temperature:

$$k_{f,k} = AT^{\beta_k} exp\left(\frac{-E_a}{RT}\right) \prod_{i=1}^{N_s} \Theta_i^{\varphi_{i,k}} exp\left(\frac{\varepsilon_{i,k}\Theta_i}{RT}\right) \quad (12)$$

For species adsorption to the catalyst surface, the sticking coefficient was used to compute the rate coefficient as:

$$k_{f,k} = \frac{\gamma}{\Gamma^{\tau}} \sqrt{\frac{RT}{2\pi M_k}} \quad (13)$$

Volumetric gas phase reactions are also included; however, their contribution is insignificant due to the low operating pressure (atmospheric) [14]. The kinetics equations were coupled with the conservation equations in the solver to consider both chemical and physical processes simultaneously.

2.6. Solver

Commercial CFD package ANSYS Fluent 13.0 software (ANSYS Inc.) was used to perform the simulation. The segregated steady state solver was selected to numerically solve the conservation equations. Second order upwind discretization scheme was employed to reduce discrete errors and improve accuracy. However the PRESTO! scheme was used for pressure since it is more appropriate to use with a porous media model. Numerical model convergence was assured by monitoring the scaled residuals and temperature variations at a cell in the vicinity of the catalyst entrance, where considerable gradients occur. Convergence criteria were set at 10^{-5} for continuity and 10^{-6} for species concentration.

3. Results and discussions

3.1. Model validation and characteristics

The CFD model of biogas reforming was validated by comparison with the experimental study by Lau et al. [12]. Fig. 3(a) shows the comparison between the experiment, CFD model and equilibrium predicted gas composition at the reactor outlet. It was found that the equilibrium model overestimates the reaction rates and leads to higher hydrogen yield as some slow reactions might not reach their equilibrium state. The model proves to have a reasonable consistency with the empirical data. The discrepancy percentage between the measured data and the corresponding CFD prediction is 7.3% for H_2, 3.5% for CH_4, 15.9% for CO, and 3.4% for CO_2.

Fig. 3(b) demonstrates the temperature profile comparison between the predicted CFD model and experimental data along the catalyst length. As illustrated, the temperature increases rapidly close to the catalyst entrance due to the exothermic oxidation reactions. Endothermic dry and steam reforming reactions cause subsequent continuing temperature decrease, as they are much slower than POX [15]. The height, width and position of the temperature peak are associated with the reactor gas feed composition and operating conditions [16]. The predicted temperature profile is in an acceptable agreement with the measured data, while the maximum discrepancy of 10.6% occurs at the temperature peak. One potential reason for this is the insufficient accuracy of the thermocouples which were used in the experiment, particularly where there is a significant temperature gradient. Moreover, in the CFD model the inlet mixture was assumed to be homogenous and the

inhibition effect of the adsorbed species was neglected, which might affect some reaction rates.

Fig. 4 shows the species concentration profile along the dimensionless length of the catalyst. Initial O_2 and CH_4 depletion is associated with catalytic oxidation reactions. CO_2 concentration is increased slightly close to the catalyst inlet, as it is a product of methane catalytic combustion. Within around 0.2 to 0.8 of the catalyst length the DRR, SRR and WGSR proceed gradually. Approximate thermodynamic equilibrium is reached at about 0.8 of the monolith length, where a negligible concentration gradient is observed. These results are in good agreement with the literature [7, 17].

3.2. Effect of O_2/CH_4 ratio

According to Lau et al. at low exhaust gas temperatures no reforming activity is observed [12]. The main reason is that the reactant enthalpy is insufficient to overcome the activation energy barrier of the reforming reactions. By providing O_2 in the reactor feed an increase in the reactor temperature can be seen due to partial oxidation and catalytic combustion of methane near the catalyst entrance (when the reactor temperature is higher than the catalyst light-off temperature) [18]. As mentioned in Section 1, in this method part of the fuel energy is released to heat up the reactor and hence promote other reforming reactions. Since oxidation reactions are relatively fast (in the range of milliseconds) and are associated with high energy release, hot spots can potentially form inside the catalyst [19]. This effect might limit the catalyst's performance and increase its deactivation.

Fig. 5 illustrates the temperature contour of the catalyst's cross section at different O_2/CH_4 ratios in the range 0.18 to 0.50. As shown in the figure, the temperature raises to a peak at about 0.14 of the catalyst bed length. Increasing the O_2/CH_4 ratio leads to a significant increase in the reactor peak temperature. Increased O_2 concentration in the feed gas promotes the oxidation reaction rates and therefore more fuel energy is released as heat. It should be mentioned that complete O_2 conversion was observed throughout all simulated operating conditions. By considering the reactor's temperature profiles in Fig. 6, it can be concluded that higher temperature peaks are followed by more significant temperature drops and improved H_2 and CO as will be discussed later; which are caused by accelerated dry and steam reforming reactions in addition to other heat transfer phenomena.

The temperature, shape and position of the hot spot in the catalyst at various O_2/CH_4 ratios are illustrated in Fig. 5. In addition, the catalyst temperature contours at different gas space velocities are shown in Fig. 7. By comparing Figs. 5 and 7 it can be established that the maximum temperature of the hot spot is associated mainly with the O_2/CH_4 ratio, while its position and length is determined by the GHSV. Shi et al. argue that increasing monolith thermal conductivity (e.g. using a metallic monolith) decreases the hot spot temperature; however, the yield of hydrogen decreases to some extent [20].

3.3. Effect of GHSV

The effect of the GHSV, which is directly related to the feed gas flow rate, on the temperature profile and reforming performance was investigated in the range 16,500 h^{-1} to 34,500 h^{-1}. As illustrated in Fig. 8, increasing the GHSV shifts the position of the peak temperature downstream of the catalyst. Although the maximum hot spot temperature

remains the same, the average catalyst temperature is slightly higher at elevated flow rates due to a more uniform temperature distribution. It was seen that the feed gas temperature at the catalyst inlet is lower at higher GHSV values; since the flow has less time to gain heat in the upstream heat-up zone. Nevertheless a similar peak of temperature compared to lower space velocities is still reached further down the catalyst at around Z/L=0.2 as fast partial oxidation reaction is still taking place and is only affected by the O_2/CH_4 ratio. Consequently, it was found that the initial temperature increase is slightly promoted by increasing the gas space velocity. This is caused mainly by improved transport of reactants to the catalyst active sites at higher velocities which leads to promoted oxidation reactions [16].

The effect of the GHSV on the final composition of the reactor can be seen by comparing Fig. 9(a) and (b). It was observed that increasing feed gas space velocity results in a lower hydrogen yield within all simulated O_2/CH_4 ratios. It should be noted that by increasing the GHSV from 16,500 h^{-1} to 32,500 h^{-1}, the residence time decreases from 0.22 s to 0.11 s (Eq. 5). Therefore the gas phase species do not have enough time to adsorb on the catalyst surface and the reactions are controlled by mass transport phenomena [21]. This effect has considerable adverse influence on DRR and SRR, since they are relatively slow processes and require adequate time to proceed.

3.4. Reforming process efficiency

The overall reforming efficiency was defined as the ratio of the reformed gas chemical power to the feed biogas power:

$$\eta(\%) = \frac{\mathrm{LHV}_{prod}\dot{m}_{prod}}{\mathrm{LHV}_{feed}\dot{m}_{feed}} \times 100\% \quad (14)$$

Where $\dot{m}_{feed}$ and $\dot{m}_{prod}$ are the mass flow rates (kg/s) of the feed gas and product gas, respectively. LHV is the lower heating value of the combustible species and is equal to 50.0 MJ/kg for CH_4, 120.9 MJ/kg for H_2 and 10.1 MJ/kg for CO. It should be noted that reforming efficiency can exceed 100%, as part of the exhaust gas energy is recovered.

The methane conversion was also defined as:

$$\mathrm{CH_4Conversion}\ (\%) = \frac{\dot{m}_{\mathrm{CH_4}\ feed} - \dot{m}_{\mathrm{CH_4}\ prod}}{\dot{m}_{\mathrm{CH_4}\ feed}} \times 100 \qquad (15)$$

As shown in Fig. 10(a), by increasing O_2 concentration the reforming efficiency decreases by approximately 15%, even though more hydrogen with higher LHV is produced at elevated O_2/CH_4 ratios. This decrease is associated mainly with methane catalytic combustion, which is more likely to occur at higher temperatures. On the other hand, Fig. 10(b) illustrates that methane conversion is directly dependent on the O_2/CH_4 ratio; since more methane oxidises due to the higher oxidant level (O_2 concentration) in feed gas [22]. Moreover, an elevated reactor temperature (caused by exothermic oxidation reactions) enhances the reforming reaction rate and consequently converts more methane into synthetic gas. By decreasing GHSV to 16,500 h^{-1} the reforming efficiency and methane conversion is slightly increased due to the promoted DRR and SRR, as discussed earlier in Section 3.3 [23, 24].

4. Conclusions

In this study, a CFD model for biogas reforming on a rhodium monolith was developed and validated using experimental data by Lau et al. The catalyst zone was considered as a porous media and a detailed kinetic model was adapted. Adequate consistency was found

between CFD prediction and experimental measurement in terms of product gas composition and reactor temperature profile. The model was then used to investigate various operating conditions of an REGR system to upgrade biogas on-board.

The results imply that the reactor's maximum local (hot spot) temperature is highly dependent on the O_2/CH_4 ratio; while GHSV affects the position and length of the hot spot. It was also concluded that for automotive applications increasing the O_2/CH_4 ratio is beneficial to trigger exothermic oxidation reactions that can promote biogas reforming when the exhaust gas temperatures are low. Furthermore, a trade-off was observed in increasing the GHSV, where a fast partial oxidation reaction were enhanced due to improved transfer phenomena to active sites and slow steam and dry reactions was limited due to lower residence time. This study shows that with a sophisticated control over parameters such as O_2/CH_4 ratio, GHSV and inlet temperature, biogas can be implemented in an REGR system to generate hydrogen enriched gas for IC engine emissions control. This work can be extended for a deeper understanding of intermediate species effect on surface reactions (e.g. inhibition, promotion).

Acknowledgments

The School of Mechanical Engineering of the University of Birmingham is gratefully acknowledged for the financial grant to M.R. Hamedi.

References

[1] Rasi S, Veijanen A, Rintala J. Trace compounds of biogas from different biogas production plants. Energy 2007;32(8):1375-80.

[2] Börjesson P, Mattiasson B. Biogas as a resource-efficient vehicle fuel. Trends Biotechnol 2008;26(1):7-13.

[3] Markard J, Stadelmann M, Truffer B. Prospective analysis of technological innovation systems: Identifying technological and organizational development options for biogas in Switzerland. Res Policy 2009;38(4):655-67.

[4] Swami Nathan S, Mallikarjuna JM, Ramesh A. An experimental study of the biogas–diesel HCCI mode of engine operation. Energy Convers Manage 2010;51(7):1347-53.

[5] Tsolakis A, Megaritis A. Partially premixed charge compression ignition engine with on-board production by exhaust gas fuel reforming of diesel and biodiesel. Int J Hydrogen Energy 2005;30(7):731-45.

[6] Abu-Jrai A, Tsolakis A, Megaritis A. The influence of H2 and CO on diesel engine combustion characteristics, exhaust gas emissions, and after treatment selective catalytic NO reduction. Int J Hydrogen Energy 2007;32(15):3565-71.

[7] Scognamiglio D, Russo L, Maffettone PL, Salemme L, Simeone M, Crescitelli S. Modelling and simulation of a catalytic autothermal methane reformer with Rh catalyst. Int J Hydrogen Energy 2012;37(1):263-75.

[8] Dalle Nogare D, Degenstein NJ, Horn R, Canu P, Schmidt LD. Modeling spatially resolved profiles of methane partial oxidation on a Rh foam catalyst with detailed chemistry. J Catal 2008;258(1):131-42.

[9] Go KS, Son SR, Kim SD, Kang KS, Park CS. Hydrogen production from two-step steam methane reforming in a fluidized bed reactor. Int J Hydrogen Energy 2009;34(3):1301-9.

[10] Deutschmann O, Schwiedernoch R, Maier LI, Chatterjee D. Natural gas conversion in monolithic catalysts: Interaction of chemical reactions and transport phenomena. Stud Surf Sci Catal 2001;136:251-58

[11] Lau CS, Tsolakis A, Wyszynski ML. Biogas upgrade to syn-gas (H_2–CO) via dry and oxidative reforming. Int J Hydrogen Energy 2011;36(1):397-404.

[12] Lau CS, Allen D, Tsolakis A, Golunski SE, Wyszynski ML. Biogas upgrade to syngas through thermochemical recovery using exhaust gas reforming. Biomass Bioenergy 2012;40(1):86-95.

[13] Levenspiel O. Chemical reaction engineering. 2nd ed. New York: Wiley; 1972.

[14] Schwiedernoch R, Tischer S, Correa C, Deutschmann O. Experimental and numerical study on the transient behavior of partial oxidation of methane in a catalytic monolith. Chem Eng Sci 2003;58(3–6):633-42.

[15] Tomishige K, Matsuo Y, Sekine Y, Fujimoto K. Effective methane reforming with CO_2 and O_2 under pressurized condition using NiO–MgO and fluidized bed reactor. Catal Commun 2001;2(1):11-5.

[16] Tsolakis A, Golunski SE. Sensitivity of process efficiency to reaction routes in exhaust-gas reforming of diesel fuel. Chem Eng J 2006;117(2):131-6.

[17] Xuan J, Leung MKH, Leung DYC, Ni M. Integrating chemical kinetics with CFD modeling for autothermal reforming of biogas. Int J Hydrogen Energy 2009;34(22):9076-86.

[18] Lee SHD, Applegate DV, Ahmed S, Calderone SG, Harvey TL. Hydrogen from natural gas: part I—autothermal reforming in an integrated fuel processor. Int J Hydrogen Energy 2005;30(8):829-42.

[19] Chen L, Hong Q, Lin J, Dautzenberg FM. Hydrogen production by coupled catalytic partial oxidation and steam methane reforming at elevated pressure and temperature. J Power Sources 2007;164(2):803-8.

[20] Shi L, Bayless DJ, Prudich ME. A CFD model of autothermal reforming. Int J Hydrogen Energy 2009;34(18):7666-75.

[21] Zhai X, Ding S, Cheng Y, Jin Y, Cheng Y. CFD simulation with detailed chemistry of steam reforming of methane for hydrogen production in an integrated micro-reactor. Int J Hydrogen Energy 2010;35(11):5383-92.

[22] Sun D, Li X, Ji S, Cao L. Effect of O_2 and H_2O on the tri-reforming of the simulated biogas to syngas over Ni-based SBA-15 catalysts. J Nat Gas Chem 2010;19(4):369-74.

[23] Xuan J, Leung DYC, Leung MKH, Ni M, Wang H. Chemical and transport behaviors in a microfluidic reformer with catalytic-support membrane for efficient hydrogen production and purification. Int J Hydrogen Energy 2012;37(3):2614-22.

[24] Avraam DG, Halkides TI, Liguras DK, Bereketidou OA, Goula MA. An experimental and theoretical approach for the biogas steam reforming reaction. Int J Hydrogen Energy 2010;35(18):9818-27.

Nomenclature

A	pre-exponential factor
CFD	computational fluid dynamics
C_p	specific heat capacity, J kg^{-1} K^{-1}
DRR	dry reforming reaction
E_a	activation energy, J mol^{-1}
F	body forces, N
GHSV	gas hourly space velocity, h^{-1}
GTL	gas to liquid
h_i	enthalpy of species i, J kg^{-1}
IMEP	indicated mean effective pressure
J_i	mass diffusion flux of species i, kg m^{-2} s^{-1}
k	thermal conductivity, W m^{-1} K^{-1}
$k_{f,k}$	forward reaction rate of reaction k, mol m^{-2} s^{-1}
K_s	total number of surface reactions
LHV	lower heating value, J kg^{-1}
$\dot{m}$	mass flow rate, kg s^{-1}
M_i	molecular weight of species i, kg mol^{-1}
N_g	total number of gas phase species
N_s	total number of surface adsorbed species
p	pressure, Pa
POX	partial oxidation reforming
R	universal gas constant, J K^{-1} mol^{-1}
R_i	depletion/creation rate of species i, mol m^{-2} s^{-1}
R-EGR	reformed exhaust gas recirculation
S_h	enthalpy source term, J kg^{-1}

S_i	species source term, mol
SRR	steam reforming reaction
t	time, s
T	temperature, K
v	velocity, m s^{-1}
WGSR	water gas shift reaction
X_i	molar concentration of species i, mol m^{-3}

Greek symbols

β	temperature exponent
γ	sticking coefficient
Γ	site density, mol m^{-2}
ε	coverage correction energy, J mol^{-1}
Θ	surface coverage fraction
ρ	density, kg m^{-3}
τ	number of sites occupied by species
$\upsilon_{i,k}$	stoichiometric coefficient of species i in reaction k
φ	coverage exponent

Table 1 – Operating conditions for biogas reforming

Table 1 – Operating conditions for biogas reforming				
Parameter	Conditions			
GHSV (h^{-1})	16,500	25,500	32,500	
O_2/CH_4 molar ratio	0.18	0.25	0.37	0.50

Table 2 – Reactor inlet composition (molar %)

Table 2 – Reactor inlet composition (molar %)					
Species	Exhaust gas	O_2/CH_4 ratio			
		0.18	0.25	0.37	0.50
CH_4	0	33.30	28.38	22.65	18.59
CO_2	5.56	24.67	21.85	18.56	16.23
O_2	13.47	5.99	7.09	8.38	9.29
H_2O	5.23	2.32	2.75	3.25	3.60
N_2	75.74	33.70	39.90	47.13	52.27

Table 3 – Surface reaction mechanism [10]

Table 3 – Surface reaction mechanism [10]		
	A (cm, mol, s)	E_a (kJ mol^{-1})
1. Adsorption		
$H_2 + Rh_{(s)} + Rh_{(s)} \rightarrow H_{(s)} + H_{(s)}$	1.00×10^{-02}	s.c.[a]
$O_2 + Rh_{(s)} + Rh_{(s)} \rightarrow O_{(s)} + O_{(s)}$	1.00×10^{-02}	s.c.[a]
$CH_4 + Rh_{(s)} \rightarrow CH_{4(s)}$	8.00×10^{-03}	s.c.[a]
$H_2O + Rh_{(s)} \rightarrow H_2O_{(s)}$	1.00×10^{-01}	s.c.[a]
$CO_2 + Rh_{(s)} \rightarrow CO_{2(s)}$	1.00×10^{-05}	s.c.[a]
$CO + Rh_{(s)} \rightarrow CO_{(s)}$	5.00×10^{-01}	s.c.[a]
2. Desorption		
$H_{(s)} + H_{(s)} \rightarrow Rh_{(s)} + Rh_{(s)} + H_2$	3.00×10^{21}	77.8
$O_{(s)} + O_{(s)} \rightarrow Rh_{(s)} + Rh_{(s)} + O_2$	1.30×10^{22}	355.2
$H_2O_{(s)} \rightarrow H_2O + Rh_{(s)}$	3.00×10^{13}	45.0
$CO_{(s)} \rightarrow CO + Rh_{(s)}$	3.50×10^{13}	133.4
$CO_{2(s)} \rightarrow CO_2 + Rh_{(s)}$	1.00×10^{13}	21.7
$CH_{4(s)} \rightarrow CH_4 + Rh_{(s)}$	1.00×10^{13}	25.1
3. Surface reactions		
$H_{(s)} + O_{(s)} \rightarrow OH_{(s)} + Rh_{(s)}$	5.00×10^{22}	83.7
$OH_{(s)} + Rh_{(s)} \rightarrow H_{(s)} + O_{(s)}$	3.00×10^{20}	37.7
$H_{(s)} + OH_{(s)} \rightarrow H_2O_{(s)} + Rh_{(s)}$	3.00×10^{20}	33.5
$H_2O_{(s)} + Rh_{(s)} \rightarrow H_{(s)} + OH_{(s)}$	5.00×10^{22}	104.7
$OH_{(s)} + OH_{(s)} \rightarrow H_2O_{(s)} + O_{(s)}$	3.00×10^{21}	100.8
$H_2O_{(s)} + O_{(s)} \rightarrow OH_{(s)} + OH_{(s)}$	3.00×10^{21}	171.8
$C_{(s)} + O_{(s)} \rightarrow CO_{(s)} + Rh_{(s)}$	3.00×10^{22}	97.9
$CO_{(s)} + Rh_{(s)} \rightarrow C_{(s)} + O_{(s)}$	2.50×10^{21}	169.0
$CO_{(s)} + O_{(s)} \rightarrow CO_{2(s)} + Rh_{(s)}$	1.40×10^{20}	121.6
$CO_{2(s)} + Rh_{(s)} \rightarrow CO_{(s)} + O_{(s)}$	3.00×10^{21}	115.3
$CH_{4(s)} + Rh_{(s)} \rightarrow CH_{3(s)} + H_{(s)}$	3.70×10^{21}	61.0
$CH_{3(s)} + H_{(s)} \rightarrow CH_{4(s)} + Rh_{(s)}$	3.70×10^{21}	51.0
$CH_{3(s)} + Rh_{(s)} \rightarrow CH_{2(s)} + H_{(s)}$	3.70×10^{24}	103.0
$CH_{2(s)} + H_{(s)} \rightarrow CH_{3(s)} + Rh_{(s)}$	3.70×10^{21}	44.0
$CH_{2(s)} + Rh_{(s)} \rightarrow CH_{(s)} + H_{(s)}$	3.70×10^{24}	100.0
$CH_{(s)} + H_{(s)} \rightarrow CH_{2(s)} + Rh_{(s)}$	3.70×10^{21}	68.0
$CH_{(s)} + Rh_{(s)} \rightarrow C_{(s)} + H_{(s)}$	3.70×10^{21}	21.0
$C_{(s)} + H_{(s)} \rightarrow CH_{(s)} + Rh_{(s)}$	3.70×10^{21}	172.8
$CH_{4(s)} + O_{(s)} \rightarrow CH_{3(s)} + OH_{(s)}$	1.70×10^{24}	80.3
$CH_{3(s)} + OH_{(s)} \rightarrow CH_{4(s)} + O_{(s)}$	3.70×10^{21}	24.3
$CH_{3(s)} + O_{(s)} \rightarrow CH_{2(s)} + OH_{(s)}$	3.70×10^{24}	120.3
$CH_{2(s)} + OH_{(s)} \rightarrow CH_{3(s)} + O_{(s)}$	3.70×10^{21}	15.1
$CH_{2(s)} + O_{(s)} \rightarrow CH_{(s)} + OH_{(s)}$	3.70×10^{24}	158.4
$CH_{(s)} + OH_{(s)} \rightarrow CH_{2(s)} + O_{(s)}$	3.70×10^{21}	36.8
$CH_{(s)} + O_{(s)} \rightarrow C_{(s)} + OH_{(s)}$	3.70×10^{21}	30.1
$C_{(s)} + OH_{(s)} \rightarrow CH_{(s)} + O_{(s)}$	3.70×10^{21}	145.5

[a] Value of sticking coefficient

Figure captions

Fig. 1 - R-EGR diagram.

Fig. 2 - Reactor schematic geometry.

Fig. 3 - Model validation at O_2/CH_4=0.5 and GHSV=25,500 h^{-1} (a) reactor outlet composition (b) temperature profile.

Fig. 4 - Average species mole fraction profiles along the catalyst length at O_2/CH_4=0.5 and GHSV=25,500 h^{-1}.

Fig. 5 - Temperature contours of the catalyst cross section at GHSV=25,500 h^{-1} (a) O_2/CH_4=0.18 (b) O_2/CH_4= 0.25 (c) O_2/CH_4=0.37 (d) O_2/CH_4=0.5.

Fig. 6 - Temperature profiles along the catalyst length at GHSV=25,500 h^{-1} and various O_2/CH_4 ratios.

Fig. 7 - Temperature contours of the catalyst cross section at O_2/CH_4=0.37 (a) GHSV=16,500 h^{-1} (b) GHSV=25,500 h^{-1} (c) GHSV=32,500 h^{-1}.

Fig. 8 - Temperature profiles along the catalyst length at O_2/CH_4= 0.37 and various GHSV.

Fig. 9 - Reactor product gas composition (a) GHSV=16,500 h^{-1} (b) GHSV=25,500 h^{-1}.

Fig. 10 - (a) Reforming efficiency (b) methane conversion at different O_2/CH_4 ratios and GHSV.

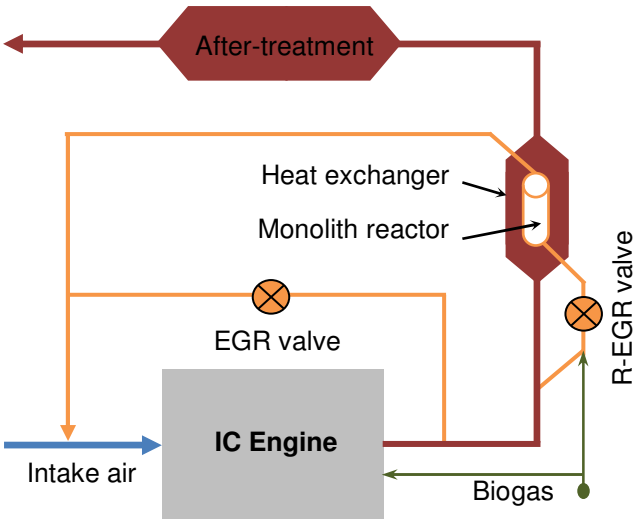
After-treatment
Heat exchanger
Monolith reactor
EGR valve
R-EGR valve
IC Engine
Intake air
Biogas

Fig. 1

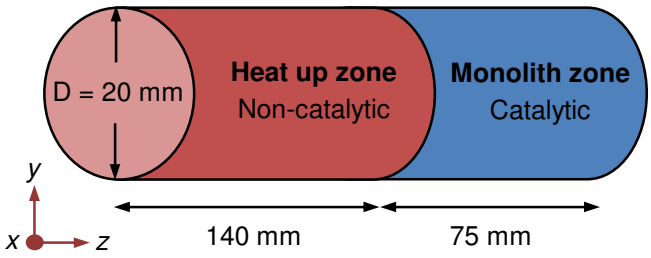
D = 20 mm
Heat up zone
Non-catalytic
Monolith zone
Catalytic
y
x
z
140 mm
75 mm

Fig. 2

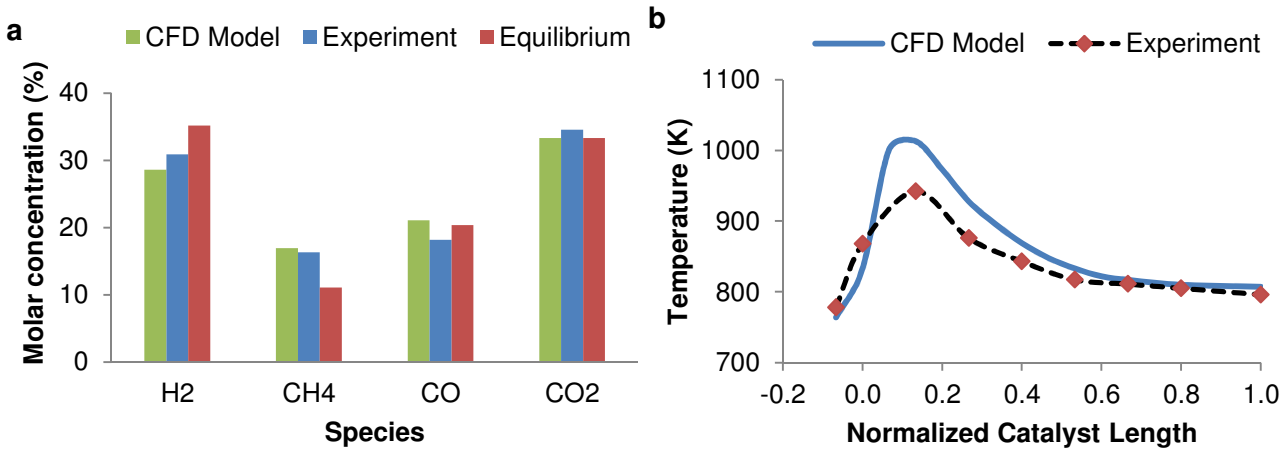
a
CFD Model
Experiment
Equilibrium
Molar concentration (%)
40
30
20
10
0
H2
CH4
CO
CO2
Species
b
CFD Model
Experiment
Temperature (K)
1100
1000
900
800
700
-0.2
0.0
0.2
0.4
0.6
0.8
1.0
Normalized Catalyst Length

Fig. 3

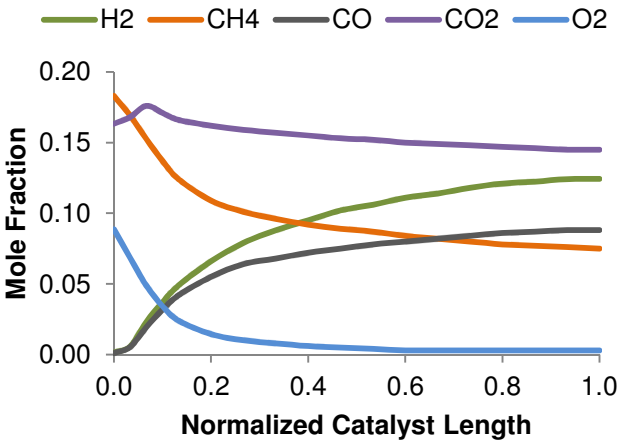
H2
CH4
CO
CO2
O2
0.20
0.15
0.10
0.05
0.00
Mole Fraction
0.0
0.2
0.4
0.6
0.8
1.0
Normalized Catalyst Length

Fig. 4

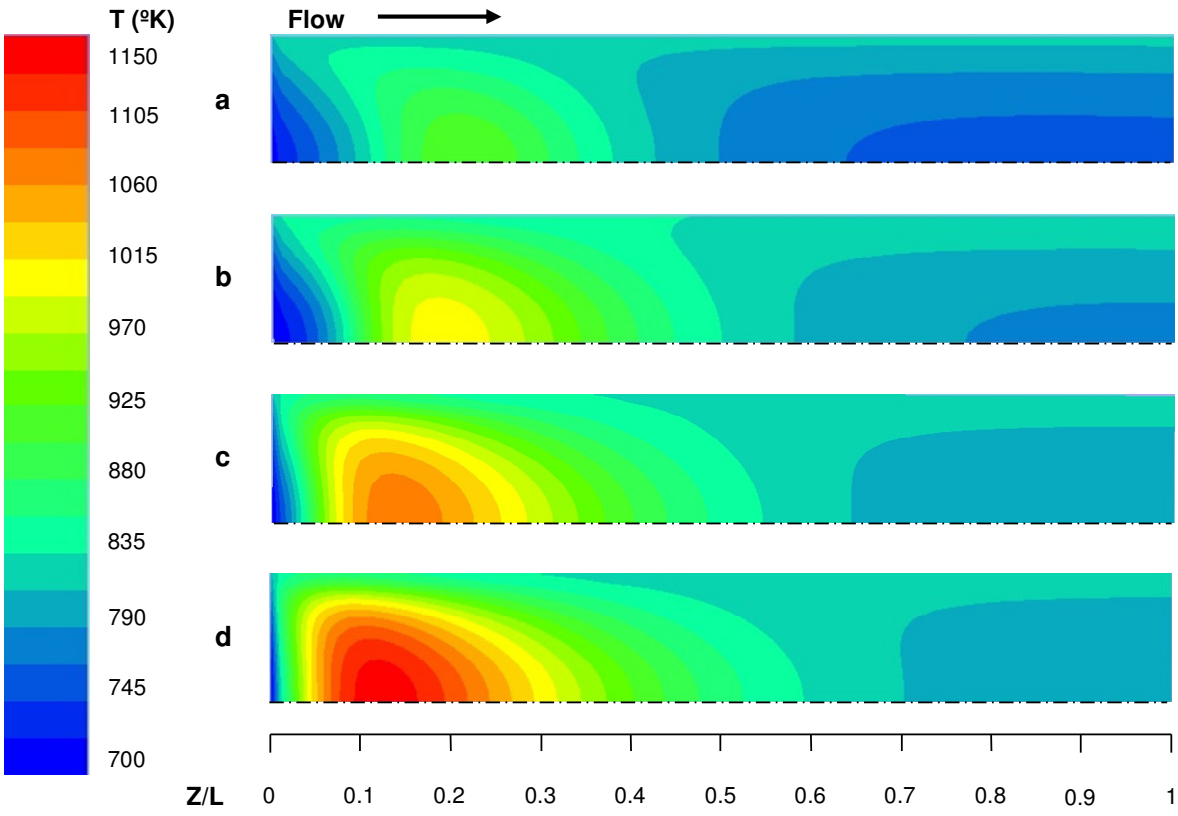
T (ºK)
1150
1105
1060
1015
970
925
880
835
790
745
700
Flow
a
b
c
d
Z/L
0
0.1
0.2
0.3
0.4
0.5
0.6
0.7
0.8
0.9
1

Fig. 5

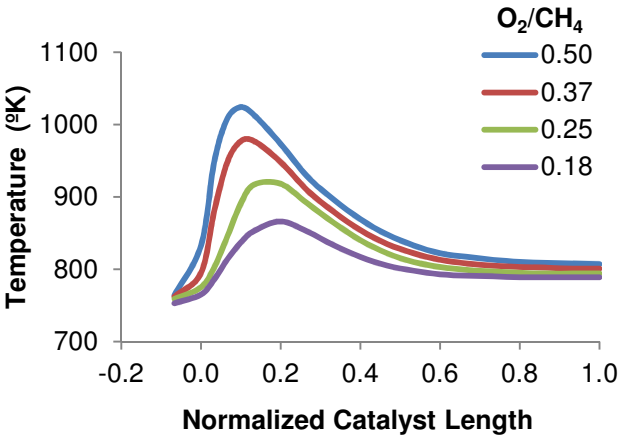
O2/CH4
0.50
0.37
0.25
0.18
Temperature (ºK)
1100
1000
900
800
700
-0.2
0.0
0.2
0.4
0.6
0.8
1.0
Normalized Catalyst Length

Fig. 6

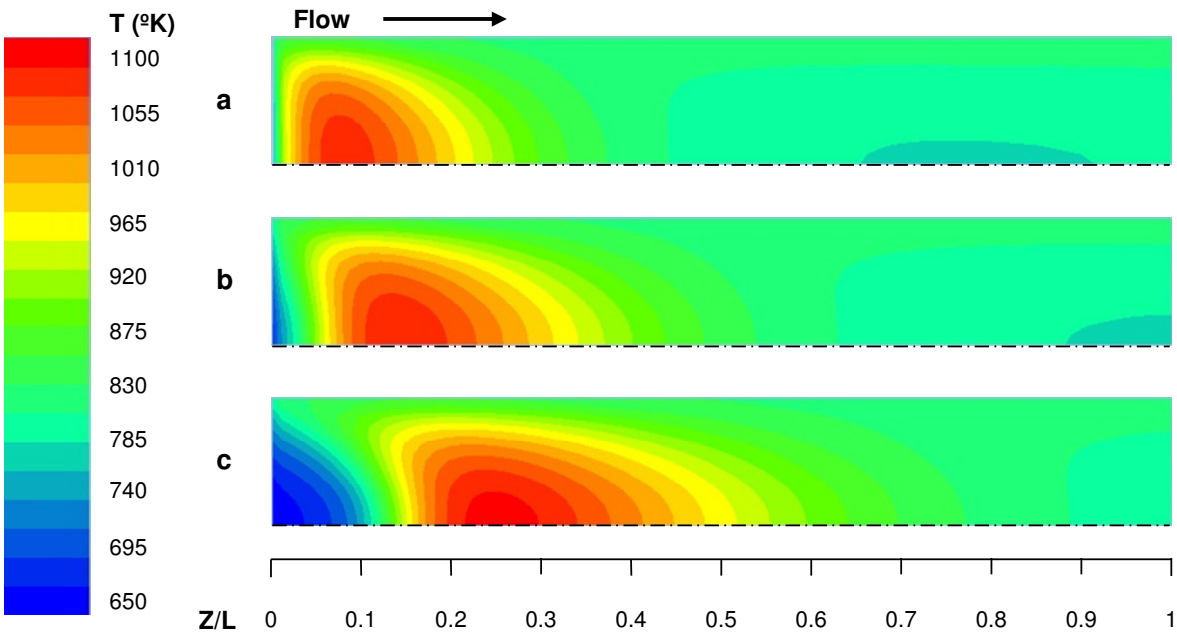
T (ºK)
1100
1055
1010
965
920
875
830
785
740
695
650
Flow
a
b
c
Z/L
0
0.1
0.2
0.3
0.4
0.5
0.6
0.7
0.8
0.9
1

Fig. 7

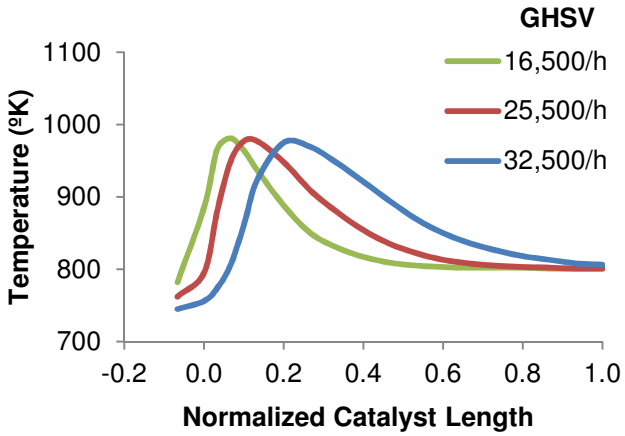
GHSV
16,500/h
25,500/h
32,500/h
Temperature (ºK)
1100
1000
900
800
700
-0.2
0.0
0.2
0.4
0.6
0.8
1.0
Normalized Catalyst Length

Fig. 8

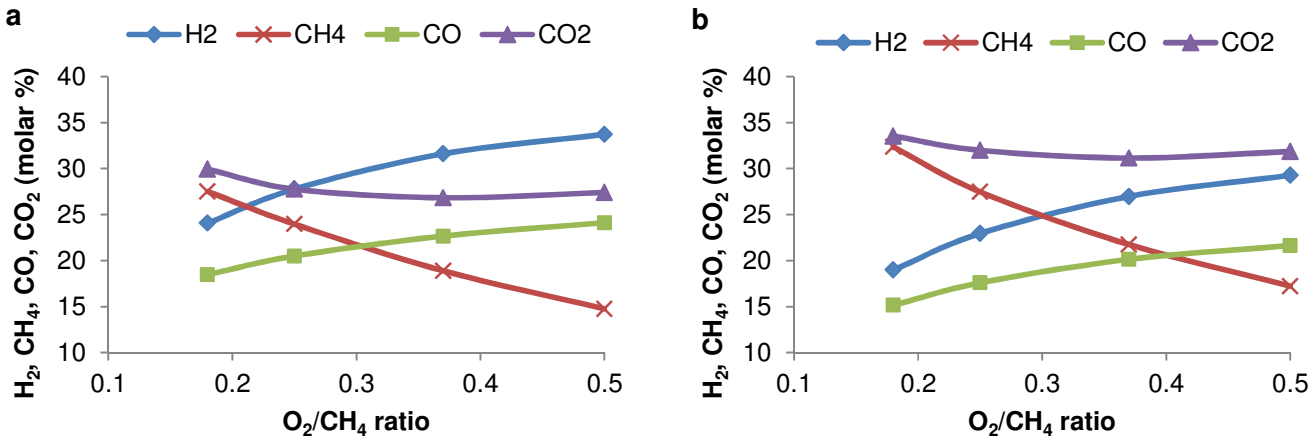
a
H2
CH4
CO
CO2
H2, CH4, CO, CO2 (molar %)
40
35
30
25
20
15
10
0.1
0.2
0.3
0.4
0.5
O2/CH4 ratio
b
H2
CH4
CO
CO2
H2, CH4, CO, CO2 (molar %)
40
35
30
25
20
15
10
0.1
0.2
0.3
0.4
0.5
O2/CH4 ratio

Fig 9

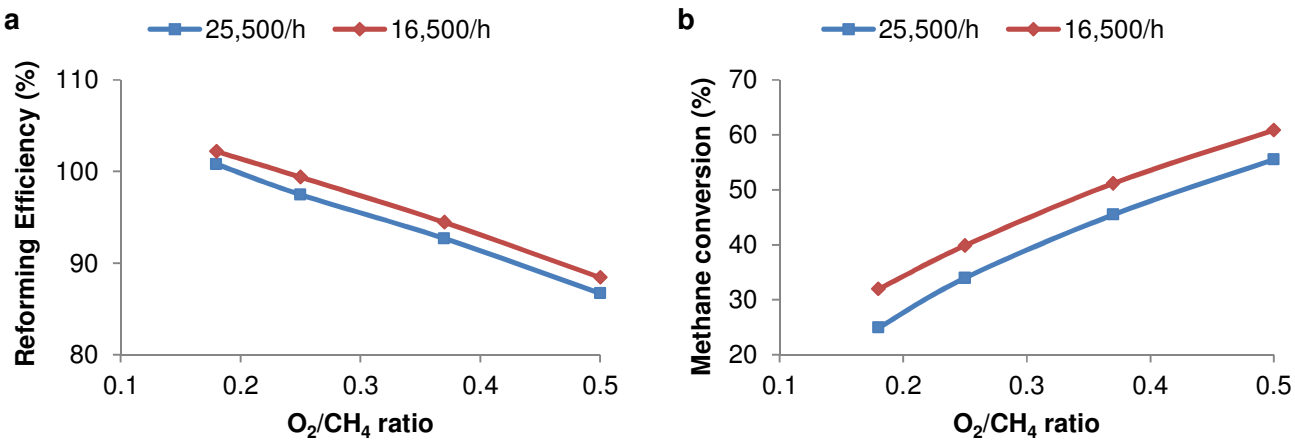
a
25,500/h
16,500/h
Reforming Efficiency (%)
110
100
90
80
0.1
0.2
0.3
0.4
0.5
O2/CH4 ratio
b
25,500/h
16,500/h
Methane conversion (%)
70
60
50
40
30
20
0.1
0.2
0.3
0.4
0.5
O2/CH4 ratio

Fig. 10